Analytical Methods

ROYAL SOCIETY OF CHEMISTRY

PAPER

View Article Online
View Journal

Cite this: DOI: 10.1039/d6ay00466k

Urease-coated polydopamine nanomotors as self-propelled biosensors for non-invasive diagnosis: detection of prostate cancer-associated miR-141 in urine

Semanur Özcan Özseven, [a] Gözde Yurdabak Karaca, [b] Lütfi Öksüz, [cd] Joseph Wang[e] and Ayşegül Uygun Öksüz *[f]

Prostate cancer (PCa) is a common health concern among men, and its early and non-invasive diagnosis is of critical importance. In this study, functionalized polydopamine/poly-L-lysine@urease (PDA/PLL@UR) nanomotors were chemically synthesized and employed for the detection of the prostate cancer-specific urinary biomarker miR-141. The catalytic decomposition of urea by urease enables autonomous propulsion of the nanomotors, enhancing the target recognition efficiency. FAM-labeled ssDNA probes were immobilized on the nanomotor surface specifically hybridized with miR-141, resulting in a significant decrease in fluorescence intensity. To further evaluate the diagnostic performance of the new mobile biosensing system, changes in the speed of nanomotors were monitored under an optical microscope. At the same time, the velocity measurements of the nanomotors were performed in PBS (pH 8) under 808 nm NIR irradiation, and the obtained results were compared with the self-propulsion velocities observed in the urea-containing medium. The nanomotors displayed self-propelled motion in urea solution, reaching an average velocity of 3.665 μm s^{-1} at 150 nM urea concentration. Calibration curves constructed from fluorescence intensity and speed data exhibited strong linear correlations with high coefficients (R^2 = 0.98 and R^2 = 0.99), and the corresponding limits of detection (LoD) were calculated as 7.5 pM and 170 pM, respectively. The specificity of the system was assessed using miR-200b and miR-21 as controls, confirming that the nanomotors selectively responded only to miR-141. Overall, the developed PDA/PLL@UR nanomotors offer a novel nanomotor-based biosensing platform for the rapid, sensitive, and non-invasive detection of PCa biomarkers in urine samples. This approach holds considerable promise for future clinical diagnostic applications.

Received 15th March 2026
Accepted 20th May 2026

DOI: 10.1039/d6ay00466k

rsc.li/methods

1 Introduction

Prostate cancer (PCa) is the second most common type of cancer worldwide and ranks as the sixth leading cause of cancer-related deaths among men.[1] By 2040, it is projected that these figures will rise globally to over 2.2 million new cases with more than 700 000 deaths.[2] In male patients, PCa is diagnosed through prostate biopsy and histological analysis, prostate-specific antigen (PSA) testing, digital rectal examination (DRE), magnetic resonance imaging (MRI), or routine health screenings.[3]

Since the 1980s, one of the most widely used diagnostic methods is the determination of PSA levels—a protein produced by the prostate gland—found in the serum of men with either PCa or benign prostatic hyperplasia (BPH). However, elevated PSA levels in both PCa and BPH patients can lead to misdiagnosis.[4] Despite issues related to false positives and overdiagnosis, PSA remains the most commonly used biomarker in the early management of PCa.[5] Due to the inherent limitations of PSA biomarkers, the search for alternative PCa biomarkers continues, with the goal of better predicting disease aggressiveness and enabling more informed treatment decisions.[6] In light of these limitations, researchers have turned to alternative diagnostic approaches and have begun investigating the potential use of biomarkers found in blood serum or urine for the diagnosis of prostate cancer (PCa).

[a]Suleyman Demirel University, Graduate School of Natural and Applied Sciences, Bioengineering, 32260 Isparta, Turkey
[b]Suleyman Demirel University, Isparta Health Services Vocational School, Medical Services and Techniques, 32260 Isparta, Turkey
[c]Suleyman Demirel University, Faculty of Engineering and Natural Sciences, Department of Physics, 32260 Isparta, Turkey
[d]PLAZMATEK, Süleyman Demirel University Technokent, No: 105, 32000 Isparta, Turkey
[e]Aiiso Yufeng Li Family Department of Chemical and Nano Engineering, University of California San Diego, La Jolla, CA 92093, USA
[f]Suleyman Demirel University, Faculty of Engineering and Natural Sciences, Department of Chemistry, 32260 Isparta, Turkey. E-mail: ayseguluygun@sdu.edu.tr

Urine samples are considered more suitable for individuals with early-stage localized PCa.[7] From the prostatic transition zone surrounding the urethra, prostate-specific cells, DNA/RNA, or protein-based biomarkers may be released into the urine.[8] Urine offers advantages as a liquid biopsy source due to its non-invasive collection method, low cost, and the potential to simultaneously sample all secretory regions of the prostate.[9] In this context, urine-based biomarker analysis stands out as a promising strategy for the early, sensitive, and non-invasive detection of prostate cancer (PCa).[10]

Nanomotors, owing to their autonomous propulsion capabilities, can actively navigate toward target biomarkers, offering faster and more selective diagnostics compared to traditional passive diffusion-based detection methods.[11] This is particularly advantageous in diseases, like prostate cancer (PCa), which often require invasive interventions. The use of nanomotors can enhance the sensitivity in detecting low-abundance biomarkers, reduce the diagnostic time, and minimize the need for invasive procedures.[12]

miRNAs are frequently used as cancer biomarkers in serum, plasma, and other body fluids; however, the analysis of miRNAs in urine remains limited. A review of the current literature indicates that four dysregulated miRNAs most consistently reported for prostate cancer (PCa) are miR-141, miR-375, miR-221, and miR-21.[13] In a study conducted by Brase *et al.* (2011), 36 prostate cancer tumor samples were compared with 36 benign prostate tissue samples, and it was observed that miR-141 and miR-375 were overexpressed in prostate tumor tissues.[14] Mharrach *et al.* investigated the potential role of miR-21 and miR-221 as biomarkers for PCa diagnosis. Analyses conducted on 50 tumors and 50 control tissue samples revealed that both miRNAs were significantly upregulated in PCa tissues. High expression levels were associated with higher Gleason scores and advanced tumor stages. The findings suggested that miR-21 and miR-221 could be used for PCa diagnosis, but further studies in non-invasive samples such as serum, blood, and urine are needed.[15]

Methods such as Polymerase Chain Reaction (PCR), microarrays, and hybridization-based techniques for the detection of miR-141 have certain limitations. qRT-PCR is restricted to single-target analysis, while microarrays offer low sensitivity and limited quantitative accuracy.[16] All these drawbacks have directed researchers to focus on miRNA electrochemical biosensors. However, these biosensors also have some disadvantages: specificity is limited due to high background signals and low signal-to-noise ratios in complex biological fluids; simultaneous detection of multiple miRNAs is challenging due to low multiplexing capability; hybridization kinetics between the target miRNA and surface-bound probes are slow, reducing sensitivity at low concentrations; the pH, ionic strength, and enzymatic activities can negatively affect sensor stability. Therefore, compared to nanomotor-based systems, which offer rapid movement and dynamic hybridization in solution, electrochemical sensors exhibit notable disadvantages.[17]

These challenges hinder the sensitive and selective detection of miR-141 in urine and limit the reliability of conventional methods. In this context, a mobile biosensor platform developed using PDA/PLL@UR nanomotors and functionalized with FAM-ssDNA aims to overcome these limitations by enabling highly specific and sensitive detection of miR-141 even at low abundance.

The small size of miRNAs, the high sequence similarity among family members, and their low abundance in biofluids make their rapid and highly accurate detection challenging, posing a significant limitation for conventional miRNA-based bioanalytical approaches. Nanomotor-based biosensors overcome these challenges by locally concentrating the target miRNAs.[18] When exposed to naturally occurring urea in urine, the nanomotors undergo a catalytic reaction in which carbon dioxide gas produced during urease-catalyzed urea hydrolysis generates a propulsive force, enabling self-guided movement toward the miR-141 biomarker.[19]

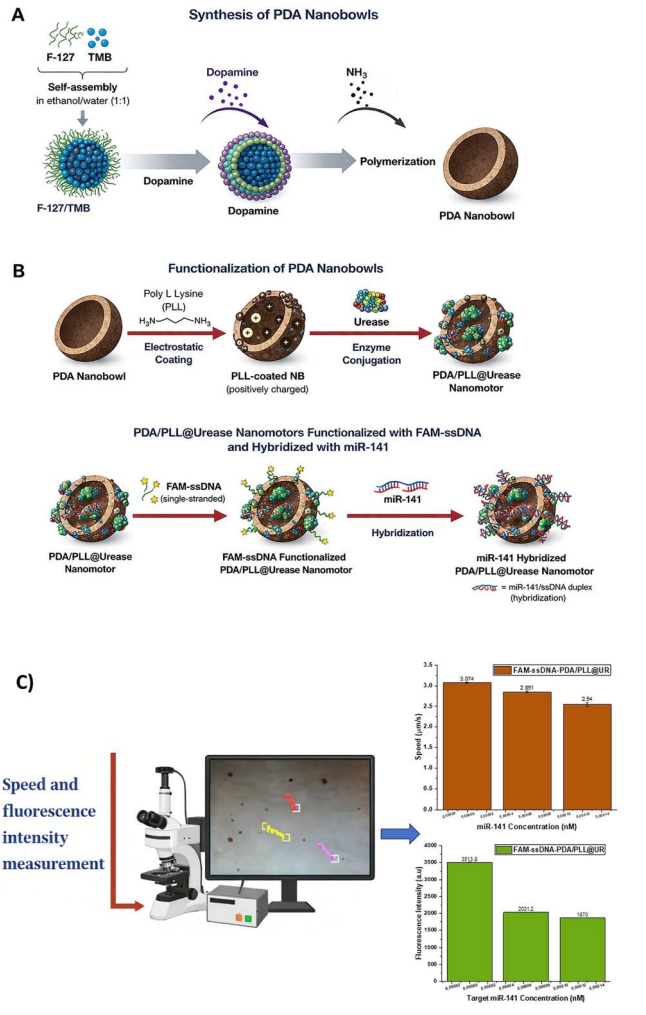

Scheme 1 Fabrication of FAM-ssDNA-PDA/PLL@UR nanomotors and detection of miR-141. (A) PDA NBs were synthesized *via* dopamine polymerization in an ethanol/water (1 : 1) system using F-127 and TMB as structure-directing agents, with ammonia as the polymerization initiator, yielding dark-brown PDA nanobowls. (B) The PDA NB surface was sequentially functionalized with PLL and urease, followed by incubation with FAM-ssDNA probes. miR-141 detection was achieved through specific hybridization with the FAM-ssDNA probes. (C) Optical readout of fluorescence intensity and reaction rate.

This study reports the synthesis of PDA/PLL@UR nanomotors that utilize diffusiophoretic propulsion generated by ammonia and carbon dioxide during urease-catalyzed urea hydrolysis, enabling the highly sensitive and selective detection of low concentrations of miR-141 in urine. PDA/PLL@UR nanomotors chemically synthesized were incubated with FAM-labeled single-stranded DNA (ssDNA) probes designed to recognize the target miR-141 (Scheme 1). The ssDNA probe was designed to hybridize with miR-141, a biomarker known in prostate cancer (PCa). Upon encountering the target miRNA, the ssDNA-functionalized PDA/PLL@UR nanomotor undergoes probe–target hybridization, enabling the diagnosis of PCa. When encountering the target miRNA, the PDA/PLL@UR nanomotor functionalized with ssDNA undergoes probe–target hybridization. This hybridization alters the conformation of the probe, causing the FAM fluorophore to move closer to the PDA surface.[20]

The decreased distance between the fluorophore and PDA enhances distance-dependent energy or electron transfer (fluorescence resonance energy transfer (FRET) or the quenching mechanism), leading to a significant reduction in fluorescence intensity.[21] This process induces changes in the physicochemical properties along with the formation of a double-stranded structure on the nanomotor surface, which in turn affects the propulsion behavior of the motor and results in measurable differences in its speed.

The limit of detection (LoD) for miR-141 was calculated based on velocity changes observed during directional movement and on fluorescence quenching resulting from hybridization between FAM-labeled ssDNA and the miR-141 sequence. An interference test using non-complementary sequences (miR-200b and miR-21) was performed to evaluate the specificity and selectivity of miR-141 detection.

2 Materials and methods/ experimental

2.1 Experimental substances and solutions

Dopamine hydrochloride (DA HCl, 98%), pluronic F-127 triblock co-polymer, 1,3,5-trimethylbenzene (TMB), 0.1% (w/v) poly-L-lysine solution in H_2O, and Sigmatrix Urine Diluent were obtained from Sigma-Aldrich. Urea (≥98.0%) was obtained from Glentham Life Sciences. Urease derived from *Canavalia ensiformis* (Jack bean) was obtained from Sigma-Aldrich. Oligonucleotides were obtained from Helix Biotechnology (Turkiye). The oligonucleotides used in the study are listed below: 6-carboxyfluorescein dye-labeled-single-stranded DNA probe (FAM-ssDNA anti-miR-141 probe): 5′-Fam-CCATCT TTACCAGACAGTGTTA-3′; target miR-141: 5′-CCA TCT TTA CCA GAC AGT GTT A-3′; miR-200b (non-complementary control): 5′-UAA UAC UGC CUG GUA AUG AUG A-3′; miR-21 (non-complementary control): 5′-UAG CUU AUC AGA CUG AUG UUG A-3.

2.2 Instrumentation

Morphological examination and elemental analysis of FAM-ssDNA/PDA/PLL@UR nanomotors were done using a scanning electron microscope (SEM-EDX), model: FEI Quanta FEG 250 (USA). To monitor and visualize the speed of the FAM-ssDNA/PDA/PLL@UR nanomotors, a Nikon Instruments Inc. Ti Optic LV100ND optical microscope was used. For the nanomotor videos, an Andor Zyla VSC-02912 camera and 40× objectives were utilized. Speed measurements were performed using a Nikon Instruments Inc. Ti Optic LV100ND model optical microscope. Based on the data obtained from this microscope, mean square displacement (MSD) and diffusion coefficients were calculated using Python and Origin software. The fluorescence intensities of the synthesized PDA nanomotors were measured using the same model of fluorescence microscope. FTIR analysis was realized in the range of 400–4000 cm^{-1} using a PerkinElmer Spectrum BX FTIR system (Beaconsfield, Buckinghamshire, HP91QA, England). X-ray photoelectron spectroscopy (XPS) measurements were carried out using a Thermo Scientific K-Alpha system equipped with a monochromatic Al Kα X-ray source and a hemispherical analyzer, and zeta potential analyses were conducted using a Malvern Panalytical Zetasizer Pro instrument.

2.3 Synthesis of polydopamine (PDA) nanobowls

The PDA NB structures were synthesized according to our previously reported method,[22] based on the work of Zhang *et al.*[23] F-127 and TMB were added to an ethanol/water (1 : 1) mixture for the synthesis of PDA. Dopamine was then introduced into the mixture, and polymerization was initiated with ammonia. The resulting dark brown solution was collected by centrifugation, washed, and stored in distilled water.

2.4 Functionalization of PDA nanobowls with PLL and urease

PDA, containing amino and phenolic hydroxyl groups, carries a negative charge at pH values above its isoelectric point and a positive charge below pH 4.[24] Therefore, when working in a PBS medium (pH 8), an increase in negative charge is observed on the PDA surface.[25] On the other hand, PLL is a cationic (positively charged) polymer that, when bound to the PDA surface, forms a charge-bearing layer.[26,27] This interaction strengthens the PDA's interaction with biomolecules. The PDA structures were washed by centrifugation at 1000 rpm for 3 minutes with ultra-pure water, and the supernatant was discarded. Then, 200 μL of PLL solution was added, and the mixture was incubated for 3 hours. In the next step, PDA/PLL nanostructures were centrifuged again at 1000 rpm for 3 minutes, and the supernatant was removed. To the PDA/PLL nanostructures, 200 μL of a 0.03 g urease solution prepared in 10 mL PBS was added, and the mixture was left to incubate overnight. The functionalization of PDA/PLL nanostructures with urease enables an enzymatic reaction that hydrolyzes urea molecules in urine, releasing ammonia and carbon dioxide.[28]

2.5 Immobilization of the FAM-ssDNA probe onto PDA/PLL@UR nanomotors

PDA/PLL@UR nanomotors were incubated with a 100 μM FAM-labeled ssDNA probe solution, prepared in a 20 mM Tris–HCl

buffer (pH 7.4) containing 100 mM NaCl, 5 mM KCl, and 5 mM $MgCl_2$, at room temperature for 30 minutes.[29] The FAM-ssDNA-PDA/PLL@UR nanomotors, with immobilized probes, were then washed with a 20 mM Tris–HCl (pH 7.4) buffer at 6000 rpm for 3 minutes.

2.6 Detection of target miRNA-141 using ssDNA-PDA/PLL@UR nanomotors

The supernatant of the FAM-ssDNA-PDA/PLL@UR nanomotors, which had been washed with a buffer solution containing 20 mM Tris–HCl (pH 7.4), 100 mM NaCl, and 5 mM $MgCl_2$, was removed. Subsequently, miRNA-141 solutions at concentrations of 100 nM, 50 nM, 25 nM, 5 nM, 2.5 nM, 1 nM, 0.25 nM, 0.1 nM, 0.05 nM, 0.01 nM, 1×10^{-3} nM, 5×10^{-4} nM, 1.25×10^{-4} nM, and 6.25×10^{-5} nM, prepared in a medium containing 20 mM Tris–HCl (pH 7.4), 100 mM NaCl, and 1 mM EDTA, were added to the nanomotors and incubated for 15 min.[30] Following incubation, each sample was washed at 6000 rpm for 3 min with a buffer solution containing 20 mM Tris–HCl (pH 7.4), 100 mM NaCl, and 1 mM EDTA. To evaluate specificity, the same procedure was also applied to the non-complementary control sequences (miR-200b and miR-21). miR-141 detection was monitored by optical microscopy based on the fluorescence intensity and speed changes of the nanomotors.

2.7 Statistical analysis

To determine differences between groups, one-way analysis of variance (one-way ANOVA) was performed. For results that were found to be statistically significant, Tukey's multiple comparison test was applied to identify which groups differed from each other. The level of statistical significance was accepted as $p < 0.05$.

For nanomotor speed, it was expected that no statistically significant difference would be observed between groups. However, even if a statistically significant difference was detected, the absence of an increase in the nanomotor speed was considered an important indicator of system stability. In this context, lower nanomotor speeds were regarded as acceptable and meaningful outcomes.

For the fluorescence intensity, a statistically significant decrease (quenching) compared to the control group was expected. The results showed that the fluorescence intensity was significantly lower than that of the control, indicating that the system exhibits stable and target-responsive behavior.

3 Results and discussion

3.1 Structural characterization

The morphological and structural features of PDA structures were comprehensively characterized using scanning electron microscopy (SEM) and energy-dispersive X-ray spectroscopy (EDX). As shown in Fig. 1a, the PDA structures typically exhibited a bowl-shaped morphology with an average diameter of 205.24 ± 22.5 nm. EDS analysis indicated that these structures were composed of approximately 65.30 wt% carbon (C), 11.46 wt% nitrogen (N), and 23.24 wt% oxygen (O) (Fig. S1). This

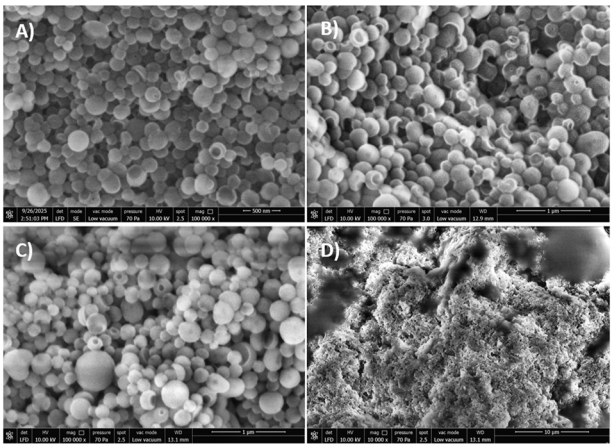

Fig. 1 SEM images of samples of (a) PDA nanoparticles; (b) PDA/PLL nanoparticles; (c and d) PDA/PLL@UR nanomotors.

elemental composition is characteristic of PDA resulting from the oxidative polymerization of dopamine monomers, with C and O originating from the catechol groups and N derived from the amine groups.[31]

The SEM image presented in Fig. 1b depicts the PDA/PLL nanostructures obtained after functionalization of PDA with poly-L-lysine (PLL).

The average diameter of these structures was measured as 234.58 ± 35.43 nm. The attachment of PLL onto the PDA surface led to an increase in polymer layer thickness, resulting in a noticeable enlargement in particle size. EDS analysis of PDA/PLL structures showed an elemental composition of 65.32% C, 11.21% N, and 23.47% O, indicating minor changes in chemical composition upon PLL functionalization (Fig. S2). The additional amino groups present in PLL are expected to directly influence the nitrogen content, while the carbon and oxygen ratios may exhibit slight variations depending on the overall matrix of the structure.[32]

Upon functionalization with urease (UR), the PDA/PLL@UR structures exhibited an average diameter of 264.05 ± 13.02 nm (Fig. 1c and d). This significant increase in particle size can be attributed to the immobilization of the enzyme, which adds extra volume to the structure. Surface-bound enzyme molecules form additional layers on the particle surface, contributing to morphological growth. EDS analysis of PDA/PLL@UR structures revealed an elemental composition of 63.67% C, 11.73% N, and 24.60% O (Fig. S3). The slight decrease in carbon content and the corresponding increase in nitrogen and oxygen content can be ascribed to the proteinaceous nature of urease.[33] Given that enzymes contain abundant amino and carboxyl groups, these functional groups are reflected in the elemental analysis as increased N and O ratios, further supporting the successful immobilization of the enzyme.[34]

The colloidal stability of PDA, PDA/PLL, PDA/PLL@UR, FAM-ssDNA-PDA/PLL@UR, and FAM-ssDNA-PDA/PLL@UR/miR-141 nanomotors was further analyzed using dynamic light scattering (DLS) in phosphate-buffered saline (PBS, pH 8) (Fig. S4).

To further corroborate the successful synthesis of the nanomotors, Fourier Transform InfraRed (FT-IR) spectroscopy was performed. Fig. S5 displays the FT-IR spectra of PDA, PDA/PLL, PDA/PLL@UR, and ssDNA-PDA/PLL@UR nanostructures. The spectra of PDA exhibit broad bands at 2973 cm^{-1} and 3337 cm^{-1}, corresponding to N–H and O–H stretching vibrations, respectively.[35] Peaks at 1634 cm^{-1} and 1454 cm^{-1} were attributed to primary amine N–H bending and dopamine aromatic C=C stretching vibrations, respectively.[36]

The successful functionalization of PDA with PLL was confirmed by the appearance of characteristic amide I (1620–1700 cm^{-1}) and amide II (1534 cm^{-1}) bands, indicating the preservation of peptide bonds and the structural integration of PLL within the nanostructure.[37] After urease functionalization of PDA/PLL structures, a minor shift was observed in the amide I band at 1650–1700 cm^{-1}, corresponding to the C=O stretching of carbonyl groups.[38] Following incubation of PDA/PLL@UR nanomotors with ssDNA, a peak at 1085 cm^{-1} was observed, which can be attributed to the symmetric stretching of phosphate groups in nucleic acids.[39] These results collectively confirm the stepwise functionalization and successful immobilization of PLL, urease, and ssDNA on the PDA nanostructures.

The surface modification process of the nanomotors was further characterized by zeta potential measurements (Fig. 2). Following functionalization of PDA nanomotors with poly-L-lysine (PLL), a synthetic polymer composed of positively charged lysine residues,[40] the zeta potential increased from −41.37 mV to −27.75 mV, indicating successful surface functionalization. Urease exhibits an isoelectric point of approximately 5.4;[41] at pH values above this, the jack bean urease hexamer acquires a net negative charge.[42] Accordingly, after functionalization with a urease solution at pH ∼7.0, the zeta potential of PDA/PLL@UR nanomotors decreased to −29.66 mV. Subsequent incubation of PDA/PLL@UR with FAM-labeled ssDNA further decreased the zeta potential to −37 mV, reflecting the contribution of the negatively charged phosphate groups (PO_2^-) of ssDNA molecules[43] and confirming successful ssDNA immobilization. Hybridization of the immobilized FAM-ssDNA with miR-141 resulted in a significant positive shift in zeta potential from −37 mV to −19 mV. Both ssDNA and miRNA possess a high negative surface potential due to their phosphate backbones. During hybridization, the close proximity of phosphate groups induces a redistribution of surface charge density, leading to a reduction in the overall negative charge on the nanomotor surface and a concomitant increase in the zeta potential.[44] This observation was further supported by studies demonstrating how conformational changes of nucleic acids influence surface electrostatic properties.[45] Additionally, the presence of miR-141 as a complementary strand effectively doubles the number of point charges, enhancing electrophoretic mobility in solution, which can contribute to increased particle velocities and higher zeta potential values.[46]

To evaluate the active motion of the nanomotors, the hydrodynamic size and fundamental diffusion behaviors were formulated, and the diffusion coefficient (D) was determined in PBS (pH 8). For spherical particles, time-dependent fluctuations in scattered light intensity were fitted to an autocorrelation function to estimate the diffusion coefficient (D) of particles.[47]

This value can then be related to the hydrodynamic diameter (d) using the Stokes–Einstein equation (eqn (1)).[48] Furthermore, using the obtained hydrodynamic diameter data, the diffusion coefficient was also calculated *via* the Stokes–Einstein equation (Fig. 3).

$$D = \frac{k_b T(\mathrm{K})}{3\pi\eta d} \quad (1)$$

Here, D represents the diffusion coefficient ($m^2\ s^{-1}$), k_b is the Boltzmann constant ($J\ K^{-1}$), T denotes the temperature (K), η is the dynamic viscosity of the medium (Pa s), and d corresponds

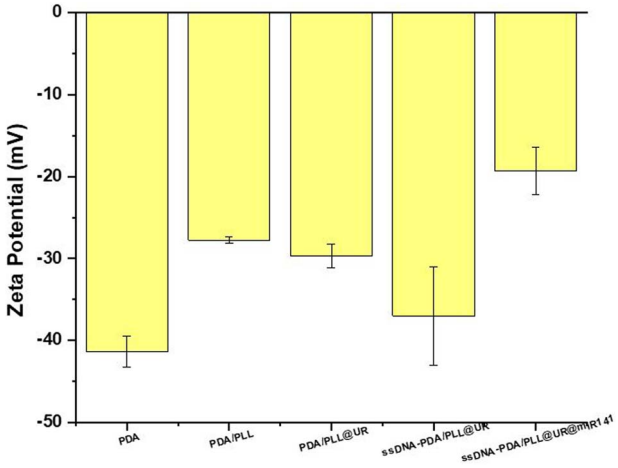

Fig. 2 Zeta potentials of PDA, PDA/PLL, PDA/PLL@UR, and FAM-ssDNA-PDA/PLL@UR nanomotors, highlighting the stepwise changes in surface charge upon sequential functionalization. (The comprehensive zeta potential analysis results of nanomotors are provided in the Supplementary Information.)

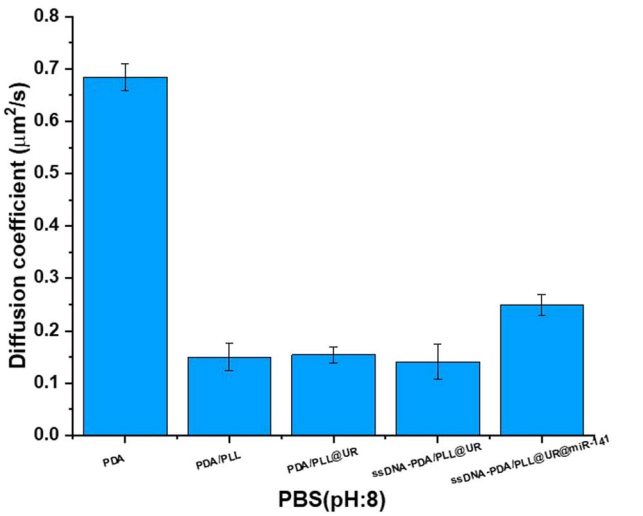

Fig. 3 Diffusion coefficient (D) calculation based on the Z-average value.

to the hydrodynamic diameter (m). All measurements were conducted at 25 °C.

According to Stokes–Einstein theory, the diffusion coefficient decreases as the hydrodynamic diameter increases. Prior to incubation, the small hydrodynamic diameter of the PDA nanomotors resulted in minimal friction and the highest diffusion coefficient. Upon binding of positively charged PLL to PDA, the hydrodynamic diameter increased, leading to a corresponding decrease in the diffusion coefficient. Subsequently, during the incubation with negatively charged urease,[49] the electrostatic interactions between opposite charges caused only a slight increase in diameter, without a significant change in the diffusion coefficient. Addition of the ssDNA probe led to a minor increase in the hydrodynamic diameter and a slight decrease in the diffusion coefficient due to the negative charges of the phosphate groups.[50] Following hybridization with miR-141, the single-stranded DNA is expected to transition from a relaxed conformation to a double-stranded, more compact structure. This compaction results in a marked reduction in the hydrodynamic diameter,[51] accompanied by an increase in the diffusion coefficient, confirming the successful recognition of miR-141 by the nanomotors.

The phase–time, total counts–zeta potential and size (d nm)–percent distribution profiles of the nanomotors are shown in Fig. S4.

X-ray photoelectron spectroscopy (XPS) was employed to investigate the elemental composition and chemical states on the surface of the nanomotors, providing insight into the success of each step in the functionalization process (Fig. 4). In XPS analysis, the O 1s peak of the PDA/PLL/urease-modified surface was observed in the range of 530–532 eV, which can be attributed to oxygen-containing species such as organic groups and peptide bonds from the enzyme.[52] After ssDNA immobilization, a new peak appeared at approximately 536 eV in the O 1s spectrum, in addition to the previously observed C=O and OH signals. The O 1s peak also shifted markedly toward a higher binding energy (~536 eV), which corresponds to the P–O bonds present in the phosphate groups of the DNA backbone. According to ref. 53, the O 1s peak typically appears around 535–536 eV when DNA covalently binds to metal oxide surfaces. This shift indicates that ssDNA was successfully immobilized on the surface and that the phosphate groups engaged in chemical interactions with the substrate. Furthermore, this change reflects a new oxygen chemistry introduced by DNA, distinct from the previous protein-based configuration. Fig. S7 shows the XPS O 1s spectra and the corresponding atomic percentages (at%) of the detected functional groups. The N 1s peaks of PDA, PDA/PLL, PDA/PLL@UR, and FAM-ssDNA-PDA/PLL@UR nanomotors were observed between 399.26 and 400.08 eV. These shifts are likely associated with different nitrogen-containing bonding environments on the PDA/PLL@UR nanomotor surface.[54] In particular, the weak peak observed at 400.08 eV in the FAM-ssDNA-PDA/PLL@UR nanomotors may correspond to protonated base structures formed upon ssDNA immobilization[55] (Fig. S8). The XPS C 1s spectra initially show a dominant C–C signal (~284.6 eV) on the PDA surface. The peak shifts to approximately 286 eV, indicating an increase in C–O–C bonds and O–C=O groups contributed by FAM-ssDNA; this change reflects the enhancement of oxygen-containing carbon groups upon PLL binding or FAM-ssDNA immobilization, confirming successful surface modification. (Fig. S9). The P 2p XPS spectrum shows a P–O peak at ~133.2 eV,[56] indicating successful immobilization and functional binding of FAM-ssDNA on the surface (Fig. S10).

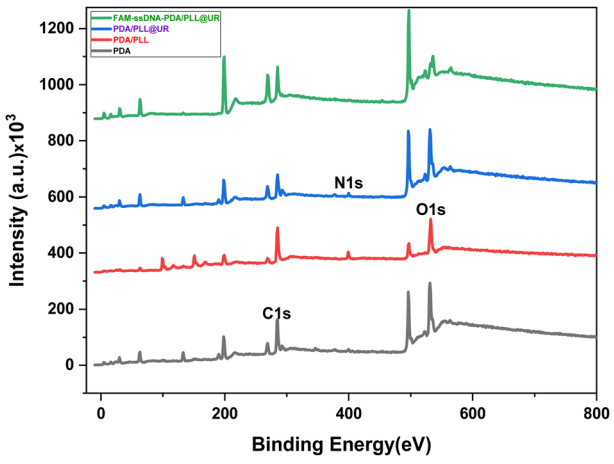

Fig. 4 X-ray photoelectron spectroscopy (XPS) survey spectra of FAM-ssDNA-PDA/PLL@UR nanomotors. The spectra confirm the presence of carbon (C 1s), nitrogen (N 1s), and oxygen (O 1s) signals, indicating the successful coating of PDA/PLL and functionalization with FAM-labeled ssDNA.

3.2 Results of optical microscopy analysis of nanomotor behavior

Although free urease-containing solution systems may exhibit some complex biological properties, they cannot ensure the controlled spread and regulation of reactions. Therefore, urease needs to be immobilized on a specific surface. This allows the enzyme to function more efficiently, the system's operation to be better controlled, and the desired reactions to be achieved.[57] In the literature, it is shown that DNA-based synthetic nanostructures can be functionalized with the urease enzyme, thereby gaining motility in the presence of biofuels (urea).[58] Moreover, it is also shown that ssDNA can bind to protein/enzyme surfaces while maintaining the enzyme's catalytic activity.[59] These findings support the use of ssDNA for functionalization with the urease enzyme in our study.

The speed measurements of the produced PDA/PLL@UR nanomotors were performed at urea concentrations of (5-10-25-50-100-150-200-250-300) nM (Fig. 5). (SI Videos S1–S5) The obtained graph shows that beyond a urea concentration of 150 nM, the reaction between urea in the solution and urease on the nanomotor reaches saturation, and further increases in urea concentration have a negligible effect on the speed.[60,61]

To examine the movement characteristics of the nanomotors at different urea concentrations, mean squared displacement (MSD) graphs over time were plotted (Fig. 6a). From these graphs, the diffusion coefficients of the nanomotors (Fig. 6b)

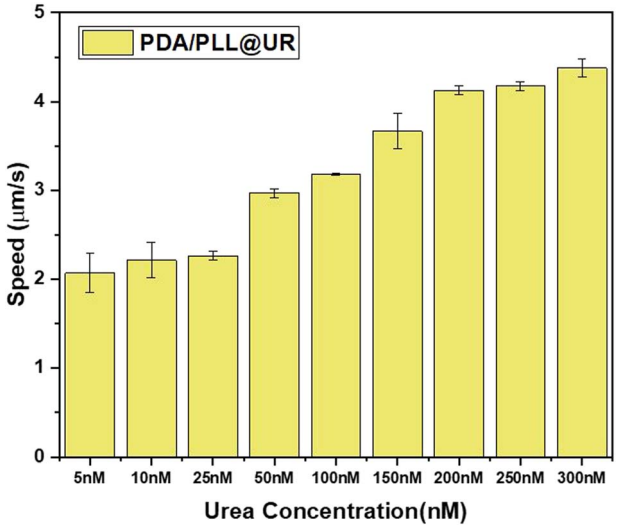

Fig. 5 Speed measurement of PDA/PLL@UR nanomotors at different urea concentrations.

were calculated, and the effect of urea concentration on motility was evaluated. The results indicated that at low urea concentrations, the movement of the nanomotors was limited, while the diffusion coefficient significantly increased with higher concentrations. This observation is consistent with recent studies.[62] These findings highlighted the effectiveness of the interaction between the nanomotors and urea, their fuel source, and its impact on their mobility. Based on the analysis, it was decided to continue the studies with a urea concentration of 150 nM, which provided both a stable movement profile and a sufficient diffusion coefficient.

To assess the mobility of the nanomotors under different conditions, their movements in urea-containing media and under near-infrared (NIR) light application were separately examined (Fig. 7). The speeds of the nanomotors were analyzed and compared using the videos obtained under both conditions (SI Videos S6 and S7). It was observed that the nanomotors moved by the propulsive force provided by the chemical reaction in the urea medium, while under NIR light, they exhibited directionally guided movement due to the photothermal effect. The speed analyses conducted in this context quantitatively revealed the effects of both conditions on the nanomotors' kinetics and allowed for a performance comparison of different stimulation mechanisms.[63] Upon reviewing the graph, it is evident that the PDA/PLL@UR nanomotors moved at a speed of 4.761 μm s^{-1} under NIR light, while they self-propelled at a speed of 3.665 μm s^{-1} in a 150 nM urea medium.

As a result of the speed analyses, it was observed that the average velocity of the nanomotors in a urea-containing medium was slightly lower than the velocity values obtained under near-infrared light. This indicates that the chemical propulsion mechanism provided by the CO_2 released during the urease-catalyzed reaction offers lower motility efficiency compared to photothermal stimulation (see eqn (2)).

$$(NH_2)_2CO + H_2O \rightarrow CO_2 + 2NH_3 \quad (2)$$

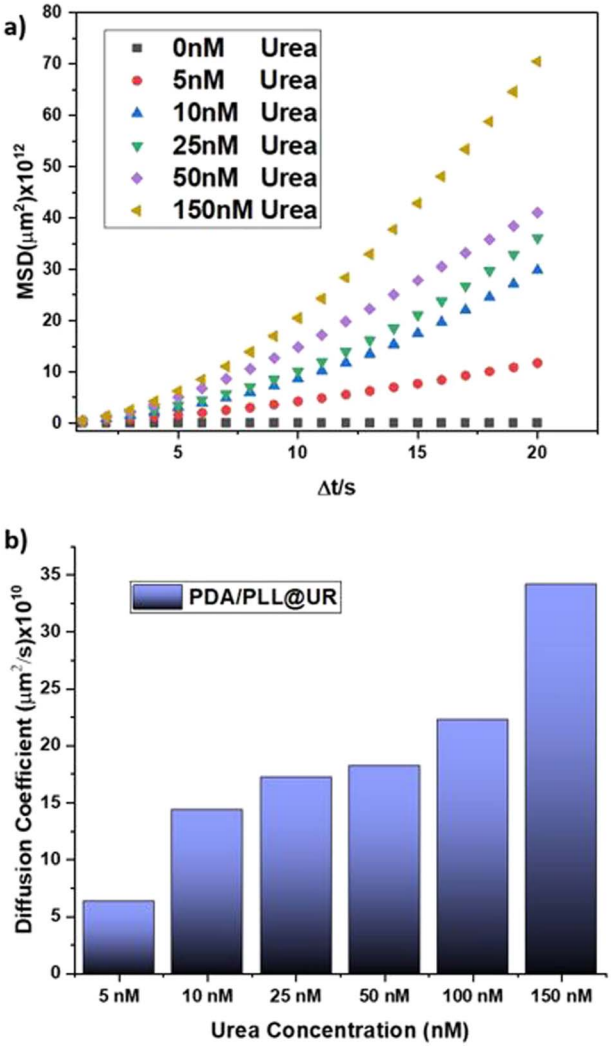

Fig. 6 (a) Mean square displacement (MSD) plots and (b) diffusion coefficient values calculated based on these data.

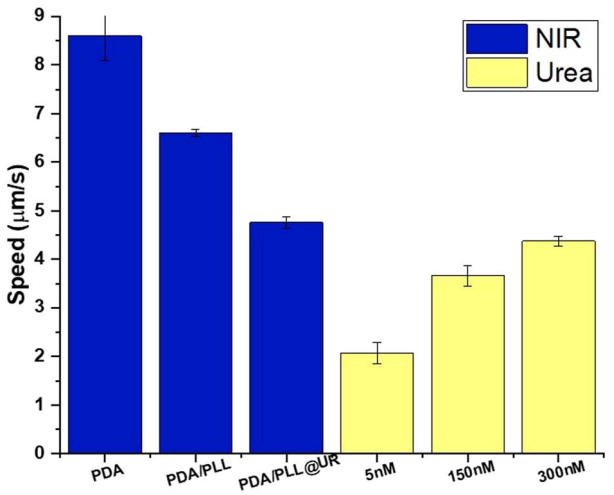

Fig. 7 Average velocity values of nanomotors in a medium containing only urea and under near-infrared (NIR) light.

These findings are important for the comparative evaluation of the impact of energy sources on nanomotor design performance.

To evaluate the diagnostic performance of the FAM-ssDNA-PDA/PLL@UR nanomotors, a calibration curve was created by measuring the fluorescence intensities corresponding to different miR-141 target concentrations (Fig. 8). The results showed a significant decrease in the fluorescence signal as the target miRNA concentration increased. This decrease is associated with the quenching of FAM fluorescence due to the hybridization of the ssDNA probe with the target miR-141 (Fig. S11). Thus, the reduction in fluorescence signal reflects a sensitive and specific diagnostic mechanism for the presence of the target nucleic acid.[64]

Furthermore, the calibration curve obtained by evaluating the fluorescence intensities corresponding to different miR-141 concentrations showed a linear relationship. The correlation coefficient for this linear region was calculated as $R^2 = 0.98$, indicating that the system responds to the target molecule with high accuracy. Based on the calibration curve, the system's limit of detection (LoD) was determined to be 7.5 pM using the 3σ/slope method (where the three times the standard deviation is divided by the slope).[65] To evaluate the diagnostic performance of FAM-ssDNA functionalized PDA/PLL@UR nanomotors, a calibration curve was generated by measuring nanomotor speeds at different miR-141 concentrations. The obtained data showed a significant decrease in nanomotor speed as the miR-141 concentration increased. This observation suggests that the hybridization of the target miRNA with the ssDNA probe increases the surface density[66] and introduces potential steric hindrance,[49] both of which may limit the motility of the nanomotor. The correlation coefficient (R^2) of the calibration curve based on the speed data was calculated to be 0.99. Based on this linear relationship, the system's limit of detection (LoD) was determined to be 170 pM (Fig. 9).

SI Fig. S9 shows the optical images of nanomotors at varying miRNA concentrations, illustrating the corresponding changes in fluorescence intensity. As observed, the fluorescence intensity gradually decreases as the miRNA concentration increases due to the hybridization of the FAM-labeled probe.

3.3 Selectivity studies

In the hybridization assays targeting miR-141, miR-200b and miR-21 were used as control miRNAs to evaluate the specificity and selectivity of the system. The control experiments were conducted under the same conditions as the target assays (identical buffer composition, temperature, and incubation times), ensuring that the observed responses were specific to miR-141.

To assess the selectivity of the FAM-ssDNA-PDA/PLL@UR nanomotors, interference tests were performed using miR-200b and miR-21 (Fig. 10). The results showed that at 5 nM concentrations of miR-200b and miR-21, the fluorescence intensity of the nanomotors exhibited only a slight decrease and remained largely stable. In contrast, a significant decrease in fluorescence was observed in the presence of 5 nM miR-141, indicating that the ssDNA probe interacts minimally with non-target miRNAs while exhibiting stronger hybridization with miR-141. These findings confirm the high specificity and selectivity of the system toward miR-141.

As another part of the selectivity assessment, the changes in nanomotor velocity in the presence of miR-200b, miR-21, and miR-141 were investigated. No significant change in nanomotor speed was observed at 5 nM concentrations of miR-200b and miR-21, whereas a notable decrease in speed was detected in the presence of 5 nM miR-141 (Fig. 11). This suggests that the ssDNA probe on the nanomotor surface hybridizes with high

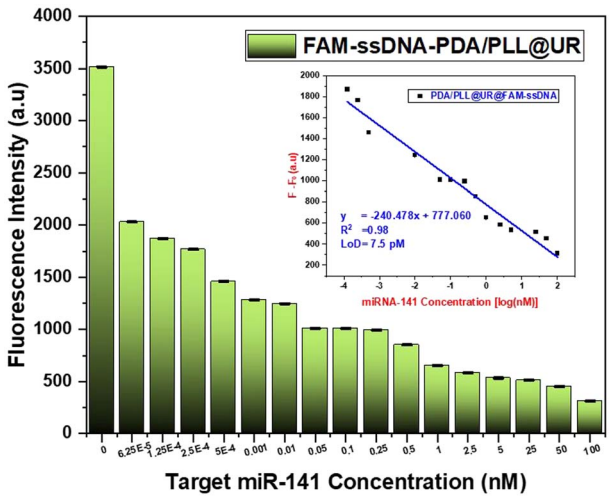

Fig. 8 Fluorescence intensity values of PDA/PLL@UR nanomotors functionalized with FAM-ssDNA corresponding to different miR-141 concentrations. Inset: calibration curve ($R^2 = 0.98$) constructed based on concentration-dependent fluorescence quenching and the calculated LoD value (7.5 pM).

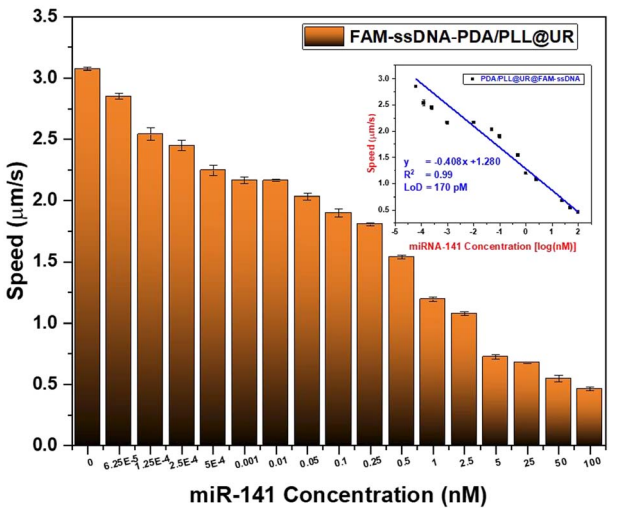

Fig. 9 Changes in the speed of nanomotors at different miR-141 concentrations. Inset: calibration curve ($R^2 = 0.99$) obtained from the speed data; LoD = 170pM.

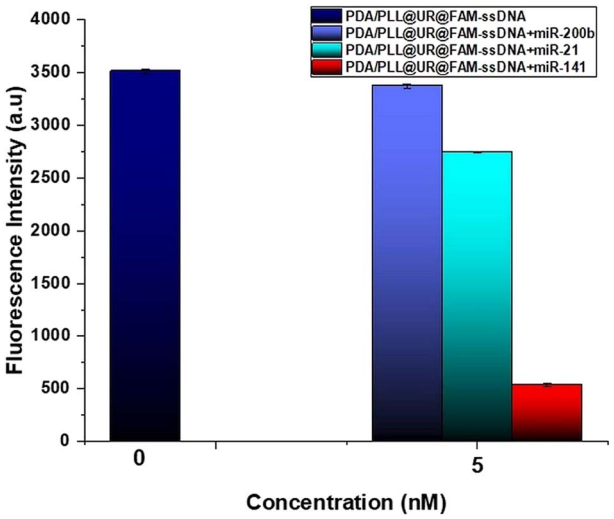

Fig. 10 Comparison of the fluorescence intensity of FAM-ssDNA-PDA/PLL@UR nanomotors in the presence of 5 nM miR-200b, miR-21 and miR-141.

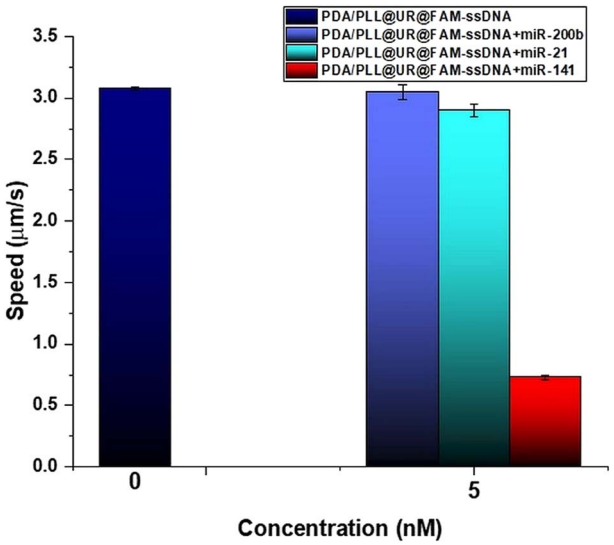

Fig. 11 Comparison of the speeds of FAM-ssDNA-PDA/PLL@UR nanomotors in the presence of 5 nM miR-200b, miR-21 and miR-141.

specificity to miR-141, and the resulting steric hindrance[67] limits its motility.

As shown in Fig. 10, pronounced fluorescence quenching was observed in the presence of miR-141, whereas only minimal changes occurred with miR-200b and miR-21, further confirming the high specificity of the nanomotor system for miR-141 recognition.

To evaluate the performance of our nanomotors in miRNA-141 detection, we compared their fluorescence response and propulsion behavior with previously reported nanomaterials. The comparison highlights the advantages of our system in terms of sensitivity, specificity, and motion-assisted target recognition, providing a clear benchmark against existing approaches (Table 1).

3.4 Studies on synthetic urine

To further investigate the propulsion behavior of the nanomotors under controlled conditions, experiments were conducted using a synthetic urine diluent with a defined composition of ions and urea. Unlike simple laboratory-prepared urea solutions, this synthetic diluent provides a homogeneous and buffered environment that mimics the ionic strength and pH of human urine. Such a setup enables a systematic evaluation of how substrate concentration, ionic composition, and enzymatic activity influence the self-propulsion of urease-functionalized nanomotors. By comparing their performance in the synthetic diluent *versus* self-prepared urea solutions, the impact of solution chemistry on nanomotor dynamics can be elucidated.

As shown in Fig. 12, the FAM-ssDNA-PDA/PLL@UR nanomotors exhibited self-propelled motion with an average velocity of 3.074 μm s^{-1} in a 150 nM urea solution, whereas a higher velocity of 4.339 μm s^{-1} was observed in the synthetic urine medium. The results demonstrate the impact of synthetic urine medium and the presence of miR-141 on the motility kinetics of the nanomotors.

The enhanced self-propulsion of nanomotors observed in synthetic urine medium, compared to laboratory-prepared urea solutions, can be attributed to several factors. The synthetic solution contains ions such as Ca^{2+}, Mg^{2+}, K^{+}, Na^{+}, and phosphate,[75] which may support the maintenance of diffusiophoretic gradients and facilitate urea hydrolysis by urease, thereby increasing the nanomotor velocity. Similarly, previous studies on electric field-driven Janus nanomotors have reported that increasing ion concentration enhances the propulsion speed, likely due to stronger electrokinetic flows at the nanomotor surface.[76] Furthermore, since urea in the synthetic solution is fully dissolved and homogeneously distributed, enzymatic hydrolysis may occur more efficiently. The buffered environment with an approximate pH of 7 also provides optimal conditions for urease activity.[77]

In the laboratory-prepared urea solution, after hybridization of phosphate backbone-bearing ssDNA with miR-141, zeta potential analysis showed a positive shift in surface charge; however, the overall nanomotor surface remained negatively charged. This indicates partial neutralization of surface negative charge density, resulting in a reduction of electrostatic repulsion forces. Such rearrangement of surface charges may affect the thickness of the electrical double layer (Debye layer) and restrict ion transport.[78] Therefore, the observed decrease in nanomotor velocity after hybridization can be attributed to these alterations in surface charge equilibrium.

Conversely, in the high ionic strength synthetic urea medium, it is suggested that positively charged ions interact electrostatically with the negatively charged phosphate groups of the ssDNA/miR-141 duplex, thereby partially compensating for the surface charge.[79] As a result, ionic gradients and urease activity are maintained, allowing diffusiophoretic motion to

Table 1 Detection performance of nanomotors for miRNA-141: fluorescence and motion analyses

Nanomaterial	Probe	Target	Detection method	Linear range	LoD	Ref.
Fe_3O_4/Au@Ur	hDNA	PCA3	Speed	1–100 pM	0.6 pM	49
İnkjet-printed gold electrodes on photopaper	Thiol-ssDNA	miR-141	Electrochemical	1 fM–100 nM	2.15 fM	17
Ur-JMNM	hDNA	miR-21 miR-182	Speed	—	29 fM 362 fM	68
Ur-JMNM	hDNA	miR-21 miR-182	Fluorescence intensity	—	4.17×10^{-13} M 1.23×10^{-12} M	68
MB-HCP immobilized on a GO-chitosan@PVP-Au nanocomposite modified GCE	DNA	miR-141	Electrochemical	2.0–5.0 $\times$ 10^5 fM	0.94 fM	69
Au nanorod/PMO JNMs	hDNA	miR-21	Speed	—	~0.018 pM	70
Bidirectional ECL miRNA-141 biosensor	Hemin/ G-quadruplex DNAzimi	miR-141	ECL (electrochemiluminescence)	10^{-17} M–10^{-9} M	7.9 aM	71
NIR-photoelectrochemical (PEC) biosensor	ssDNA	miR-155	Speed	0.1 fM–100 pM	65.77 aM	72
Integrated hairpin-based electrochemical nano-biosensor	MB-HCP+ Fc-AP-21	miR-141 miR-21	Electrochemical	2.0 fM–10^5 fM	0.89 fM 1.24 fM	73
W_5O_{14}/PEDOT-Pt	ssDNA	FAM-miR-21	Fluorescence intensity	0.1–100 nM	0.028 nM	29
An electrochemical miRNA sensor based on a screen-printed gold electrode (SPGE)	DNA	miR-21	Electrochemical		2 nM	74
PDA/PLL@UR	FAM-ssDNA	miR-141	Speed	100 pM–100 nM	7.5 pM	This work
PDA/PLL@UR	FAM-ssDNA	miR-141	Fluorescence intensity	100 pM–100 nM	170 pM	This work

continue without a significant change in the propulsion speed. The results demonstrate the effects of both the medium composition and the presence of miRNA on the fluorescence signals of the nanomotors.

In synthetic urine and 150 nM urea solution media, the initial fluorescence intensities of FAM-ssDNA-PDA/PLL@UR nanomotors were measured as ≈2410 a.u. and ≈3514 a.u., respectively, and in the presence of miRNA, the fluorescence intensities of the nanomotors in the same media were determined as 394 a.u. and 535 a.u., respectively (Fig. 13). These findings demonstrate the influence of both the medium composition and the presence of the target miRNA on the fluorescence responses of the nanomotors. Fluorescence intensity measurements revealed that, in the absence of the target molecule, the average fluorescence intensity (FI) in the laboratory urea solution was higher than that in the synthetic

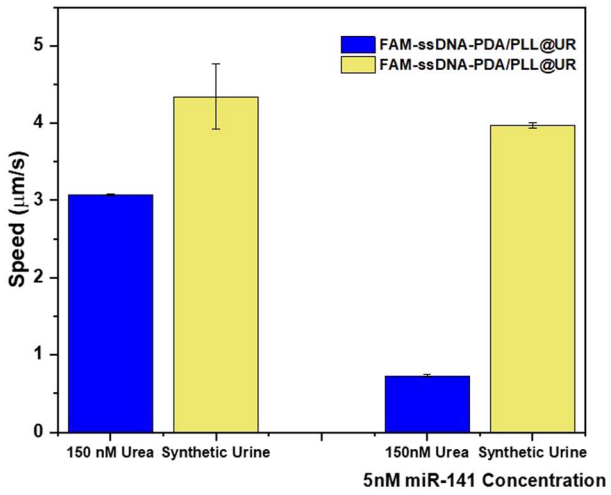

Fig. 12 Comparison of the average velocities of FAM-ssDNA-PDA/PLL@UR nanomotors in 150 nM urea solution and synthetic urine medium, and analysis of the corresponding speed changes in the same medium in the presence of 5 nM miR-141.

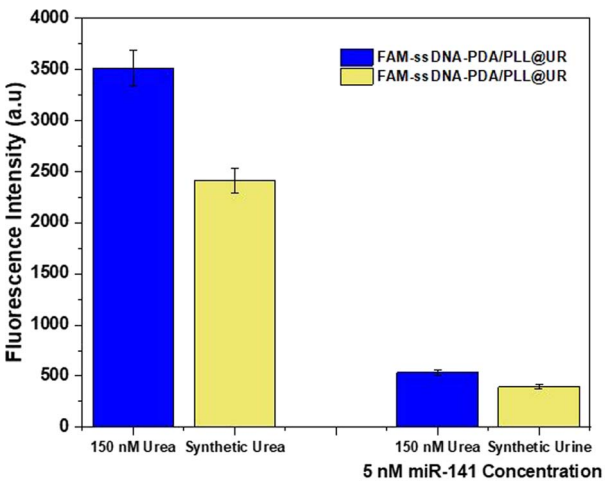

Fig. 13 Comparison of the fluorescence intensity of FAM-ssDNA-PDA/PLL@UR nanomotors in 150 nM urea solution and synthetic urine medium, and analysis of the corresponding fluorescence intensity changes in the same medium in the presence of 5 nM miR-141.

urine medium. This difference may be attributed to the interaction between the increased ionic strength and the negatively charged ssDNA chains, which reduces the light-emission efficiency of the fluorophore.[80] Upon the addition of miR-141, hybridization-induced fluorescence quenching increased markedly, confirming the target-specific recognition capability of the nanomotors. Overall, a significant decrease in ssDNA fluorescence was observed in both environments, with a stronger quenching effect in synthetic urine solution. These results demonstrate that the nanomotors can selectively detect miR-141 and can be effectively applied for urine-based prostate cancer diagnosis.

3.5 Stability evaluation of the nanomotor system

According to the ANOVA results presented in Table S1, no statistically significant effect of time on nanomotor speed was observed ($p > 0.05$), and the H_0 hypothesis was accepted. This indicates that the nanomotors maintained stable motility behavior both within a single day and over multiple days.

In contrast, the fluorescence intensity was found to change significantly over time ($p < 0.05$). This variation is attributed to fluorescence quenching associated with the hybridization process occurring on the nanomotor surface.

The Tukey HSD analyses (Fig. S14) supported these findings; no significant differences were observed between groups for nanomotor speed, whereas significant differences were detected for fluorescence intensity. The interday analysis results (Fig. S15) were also consistent with these findings, indicating a stable nanomotor speed, while fluorescence exhibited time-dependent variation.

4 Conclusions

In summary, this study successfully demonstrated the development of urease-powered FAM-ssDNA-PDA/PLL@UR nanomotors for the non-invasive detection of urinary miR-141, a clinically relevant biomarker for prostate cancer. Comprehensive physicochemical characterization confirmed the successful stepwise functionalization of the nanomotors, which enabled efficient enzymatic propulsion and highly selective target recognition. The nanomotors exhibited stable diffusiophoretic motion in synthetic urine and showed high selectivity toward miR-141, even in the presence of competing miRNA sequences, as evidenced by both motility behavior and fluorescence responses.

Although the sensing performance of the nanomotor platform was evaluated in a urine-mimicking synthetic urine medium, this environment does not fully reproduce the biochemical complexity of real human urine. Therefore, further studies are required to evaluate performance in real urine samples, assess long-term stability and reproducibility, and investigate the influence of environmental parameters such as ionic strength, pH, and temperature. Accordingly, future work will focus on the analysis of spiked human urine and clinical urine samples to assess matrix effects, analytical recovery, and diagnostic applicability under realistic conditions.

Overall, the findings indicate that urease-powered nanomotors represent a promising platform for rapid, selective, and reliable urine-based biosensing. This work lays the foundation for future clinical translation and supports the broader potential of enzyme-assisted nanomotors in diagnostic and biomedical applications.

Author contributions

Semanur Özcan Özseven: formal analysis, methodology, investigation, resources, data curation, writing – original draft, visualization. Gözde Yurdabak Karaca: methodology, writing – review & editing. Lütfi Öksüz: conceptualization, writing – review & editing. Joseph Wang: review & editing. Ayşegül Uygun Öksüz: methodology, supervision, writing – review & editing, project administration.

Conflicts of interest

There are no conflicts to declare.

Data availability

The data supporting the findings of this study are available in the supplementary information (SI) accompanying this article.

Supplementary information is available. See DOI: https://doi.org/10.1039/d6ay00466k.

Acknowledgements

This study was financially supported by the Süleyman Demirel University Scientific Research Projects Coordination Unit (BAP) under project number FDK-2024-9457 and by TÜBİTAK 1002 – B Emergency Support Module under project number 125M773.

Notes and references

1 V. Devi, V. Chaudhary, M. Sharma, S. Kumari, K. Murti, S. Meenakshi and B. Pal, in *Biological Trace Element Research*, Springer, 2025, vol. 203, pp. 4479–4488.
2 K. M. Chan, J. M. Gleadle, M. O'Callaghan, K. Vasilev and M. MacGregor, *Springer Nature*, 2022, **25**(1), 39–46.
3 M. Sekhoacha, K. Riet, P. Motloung, L. Gumenku, A. Adegoke and S. Mashele, *Molecules*, 2022, **27**(17), 5730.
4 H. Van Poppel, T. Albreht, P. Basu, R. Hogenhout, S. Collen and M. Roobol, *Nat. Rev. Urol.*, 2022, **19**(9), 562–572.
5 X. Filella and L. Foj, *Int. J. Mol. Sci.*, 2016, **17**(11), 1784.
6 S. Saini, *Cell. Oncol.*, 2016, **39**(2), 97–106.
7 C. Liao, Z. Wu, C. Lin, X. Chen, Y. Zu, W. Zhao, X. Li, G. Huang, B. Xu, G. E. Briganti, Y. Qi, X. Wang, T. Zeng, A. Wuethrich and H. Zou, *Smart Med.*, 2023, **2**(1), e20220020.
8 S. Plas, F. Melchior, G. P. Aigner, M. Frantzi, J. Pencik, M. Kafka and I. Heidegger, *Crit. Rev. Oncol. Hematol.*, 2025, 210.
9 J. Clark, R. Hurst, M. S. Winterbone, H. Pahndha, A. Perry, S. McGrath, R. Morgan, A. E. Connor, A. C. Jordan, D. Winrow and C. Cooper, *J. Urol.*, 2021, **2**(3), 159–170.

10 M. Rigau, M. Olivan, M. Garcia, T. Sequeiros, M. Montes, E. Colás, M. Llauradó, J. Planas, I. de Torres, J. Morote, C. Cooper, J. Reventós, J. Clark and A. Doll, *Int. J. Mol. Sci.*, 2013, **14**(6), 12620–12649.
11 J. Wang, *Biosens. Bioelectron.*, 2016, **76**, 234–242.
12 Z. Liang, Y. Tu and F. Peng, *Adv. Healthcare Mater.*, 2021, **10**(8), 1–15.
13 N. Sharma and M. M. Baruah, *Clin. Transl. Oncol.*, 2019, **21**(2), 126–144.
14 J. C. Brase, M. Johannes, T. Schlomm, M. Fälth, A. Haese, T. Steuber, T. Beissbarth, R. Kuner and H. Sültmann, *Int. J. Cancer*, 2011, **128**, 608–616.
15 I. Mharrach, K. A. Tadlaoui, M. Aqerrout, A. Laraqui, A. Ameur, A. el Ghazzaly, K. Ennibi and M. M. Ennaji, *Mol. Clin. Oncol.*, 2025, **22**(5), 40.
16 R. M. Graybill and R. C. Bailey, *Anal. Chem.*, 2016, **88**(1), 431–450.
17 A. Hunt and G. Slaughter, *Chemosensors*, 2025, **13**(7), 242.
18 I. Gessner, J. W. U. Fries, V. Brune and S. Mathur, *J. Mater. Chem. B*, 2021, **9**(1), 9–22.
19 S. Panja and D. J. Adams, *Chem.–Eur. J.*, 2021, **27**(35), 8928–8939.
20 X. Xue, H. Persson and L. Ye, *Microchim. Acta*, 2024, **191**, 180.
21 X. Li, T. Wang, Y. Luo, A. M. Asiri, S. Chen and X. Sun, *ChemBioChem*, 2020, **21**(6), 801–806.
22 S. Özcan Özseven, A. Türker, G. Yurdabak Karaca and A. Uygun Öksüz, *Emerg. Mater.*, 2025, **8**, 6479–6489.
23 Y. Zhang, K. Zhang, H. Yang, Y. Hao, J. Zhang, W. Zhao, S. Zhang, S. Ma and C. Mao, *ACS Appl. Mater. Interfaces*, 2023, **15**(11), 14099–14110.
24 Y. Liu, K. Ai and L. Lu, *Chem. Rev.*, 2014, **114**, 5057–5115.
25 Y. Ding, S. Su, R. Zhang, L. Shao and Y. Zhang, *Biomaterials*, 2017, **113**, 243–252.
26 I. Naassaoui and A. Aschi, *J. Macromol. Sci. B*, 2019, **58**, 673–688.
27 L. Cao, D. Tian, B. Lin, W. Wang, L. Bai, H. Chen and L. Yang, *Int. J. Biol. Macromol.*, 2021, **184**, 259–270.
28 X. Liu, Y. Wang, Y. Peng, J. Shi, W. Chen, W. Wang and X. Ma, *ACS Nano*, 2023, **17**(23), 24343–24354.
29 G. C. Cogal, G. Y. Karaca, E. Uygun, F. Kuralay, L. Oksuz, M. Remskar and A. U. Oksuz, *Anal. Chim. Acta*, 2020, **1138**, 69–78.
30 G. Y. Karaca, F. Kuralay, E. Uygun, K. Ozaltin, S. E. Demirbuken, B. Garipcan, L. Oksuz and A. U. Oksuz, *ACS Appl. Nano Mater.*, 2021, **4**(4), 3377–3388.
31 Y. Kim and J. Kim, *Polymers*, 2020, **12**(6), 1410.
32 L. Stagi, M. Sini, D. Carboni, R. Anedda, G. Siligardi, T. M. Gianga, R. Hussain and P. Innocenzi, *Sci. Rep.*, 2022, **12**(1), 19719.
33 M. A. Pearson, I. S. Park, R. A. Schaller, L. O. Michel, P. A. Karplus and R. P. Hausinger, *Biochemistry*, 2000, **39**(29), 8575–8584.
34 B. Sujoy and A. Aparna, *Eur. Sci. J.*, 2013, **9**(21), 1584.
35 B. Yi, L. Yu, H. Tang, W. Wang, W. Liu and Y. Zhang, *Appl. Mater. Today*, 2021, **25**, 101198.
36 L. Tan, T. Zhu, Y. Huang, H. Yuan, L. Shi, Z. Zhu, P. Yao, C. Zhu and J. Xu, *Advanced Science*, 2024, **11**(10), 2308153.
37 M. Rozenberg and G. Shoham, *Biophys. Chem.*, 2007, **125**(1), 166–171.
38 M. Arshad, M. Jadoon, Z. Iqbal, M. Fatima, M. Ali, K. Ayub, A. M. Qureshi, M. Ashraf, M. N. Arshad, A. M. Asiri, A. Waseem and T. Mahmood, *J. Mol. Struct.*, 2017, **1133**, 80–89.
39 M. L. Castilho, L. S. Vieira, A. P. C. Campos, C. A. Achete, M. A. G. Cardoso and L. Raniero, *Sens. Actuators, B*, 2015, **215**, 258–265.
40 I. Khmara, M. Koneracka, M. Kubovcikova, V. Zavisova, I. Antal, K. Csach, P. Kopcansky, I. Vidlickova, L. Csaderova, S. Pastorekova and M. Zatovicova, *J. Magn. Magn. Mater.*, 2017, **427**, 114–121.
41 B. Somturk, I. Yilmaz, C. Altinkaynak, A. Karatepe, N. Özdemir and I. Ocsoy, *Enzyme Microb. Technol.*, 2016, **86**, 134–142.
42 H. Kim, F. Hassouna, F. Muzika, M. Arabacı, D. Kopecký, I. Sedlářová and M. Šoóš, *J. Mater. Sci.*, 2019, **54**(24), 14884–14896.
43 Y. Matsuura, S. Arakawa and M. Okamoto, *Appl. Clay Sci.*, 2014, **101**, 591–597.
44 P. S. Kuhn, M. C. Barbosa and Y. Levin, *Phys. Stat. Mech. Appl.*, 1999, **269**(2–4), 278–284.
45 P. S. Nial and U. Subudhi, *Int. J. Biol. Macromol.*, 2024, **266**(Part 1), 131238.
46 E. L. C. J. Blundell, R. Vogel and M. Platt, *Langmuir*, 2026, **32**(4), 1082–1090.
47 K. K. Dey, X. Zhao, B. M. Tansi, W. J. Méndez-Ortiz, U. M. Córdova-Figueroa, R. Golestanian and A. Sen, *Nano Lett.*, 2015, **15**(12), 8311–8315.
48 A. McGlasson and L. C. Bradley, *Small*, 2021, **17**(52), 2104926.
49 P. Dou, Q. Liu, M. Chen, W. Xu, H. Zhou, X. Zhang, C. Jiang, Y. Zhang, S. Li, L. Mao, H. Wang, S. Zheng and K. Xu, *Sens. Actuators, B*, 2025, **426**, 137051.
50 G. Mishra and Y. Levy, *Proc. Natl. Acad. Sci. U. S. A.*, 2015, **112**(16), 5033–5038.
51 G. Yang and Y. Wang, *Methods Mol. Biol.*, 2018, **1837**, 161–176.
52 Thermo Fisher Scientific, "Oxygen XPS Periodic Table," Thermo Fisher Scientific Learning Center, Binding energies of common chemical states of O 1s, available at: https://www.thermofisher.com/us/en/home/materials-science/learning-center/periodic-table/non-metal/oxygen.html, accessed on October 14, 2025.
53 S. R. Dugasani, B. Gnapareddy, M. R. Kesama, S. Jeon, J. H. Jeong and S. H. Park, *AIP Adv.*, 2019, **9**(1), 015011.
54 A. Landge, M. Pant, S. Arote, Y. Hase, A. Pathan, S. Rahane, M. Chopade, M. Kurane, A. Kakade, S. Bhosale, P. Vairale, S. P. Patole and S. Jadkar, *Mater. Sci. Eng. B*, 2026, **324**(Part B), 119066.
55 J. C. González-Olvera, M. Durec, R. Marek, R. Fiala, M. Morales-García, R. J. del, E. González-Jasso and R. C. Pless, *ChemBioChem*, 2018, **19**(19), 2088–2098.
56 C. D. Wagner, *The NIST X-Ray Photoelectron Spectroscopy (XPS) Database, National Institute of Standards and Technology*, NIST Technical Note 1289, 1991, p. 69.

57 S. Haranal, V. A. Ranganath and I. Maity, *J. Mater. Chem. B*, 2025, **13**, 4252–4278.
58 T. P. Padial, E. del Grosso, S. Gentile, L. B. Pellejero, R. Mestre, L. J. M. M. Paffen, S. Sánchez and F. Ricci, *J. Am. Chem. Soc.*, 2024, **146**(18), 12664–12671.
59 I. Murphy, K. Bobilev, D. Hayakawa, E. Ikonen, T. E. Videbæk, S. Dalal, W. W. Ahmed, J. L. Ross and W. B. Rogers, *PLoS One*, 2025, **20**(4), e0319790.
60 W. W. Li, Z. L. Yu and J. Jia, *J. Pharm. Anal.*, 2025, **15**(3), 101095.
61 X. Ma, X. Wang, K. Hahn and S. Sánchez, *ACS Nano*, 2016, **10**(3), 3597–3605.
62 C. Hua, Z. Lu, W. Cui, W. Ren, Y. Xu, J. Li, X. Zhao, S. Zhao, P. Kang and Y. Cui, *Microchim. Acta*, 2026, **193**(2), 110.
63 Y. Liu, L. Zhang, F. Ouyang, C. Xue, X. Zhao, T. Wang, Z. Pei and Q. Shuai, *Adv. Healthcare Mater.*, 2024, **13**(17), 2304086.
64 G. T. Hwang, *Molecules*, 2018, **23**(1), 124.
65 J. Guo, Y. Li, B. Wang, W. Chen, S. Chen, S. Liu, X. Ma and J. Guo, *Microchim. Acta*, 2022, **189**(12), 468.
66 J. H. Monserud and D. K. Schwartz, *ACS Nano*, 2014, **8**(5), 4488–4499.
67 J. X. Dong, S. M. Zhang, Y. L. Zhang, Y. J. Fan, Y. L. Li, M. Su, Z. G. Wang, S. G. Shen, Z. F. Gao, Q. Wei and F. Xia, *Anal. Chem.*, 2024, **96**(36), 14471–14479.
68 H. Zhou, Q. Liu, M. Chen, Y. Xie, W. Xu, X. Zhang, C. Jiang, P. Dou, Z. Fang, H. Wang and S. Zheng, *ACS Sensors*, 2025, **10**(2), 1155–1165.
69 A. Khodadoust, N. Nasirizadeh, R. A. Taheri, M. Dehghani, M. Ghanei and H. Bagheri, *Microchim. Acta*, 2022, **189**(6), 213.
70 M. Chen, E. Ma, Y. Xing, H. Xu, L. Chen, Y. Wang, Y. Zhang, J. Li, H. Wang and S. Zheng, *ACS Sensors*, 2023, **8**(2), 757–766.
71 Z. H. Xu, H. Wang, J. Wang, W. Zhao, J. J. Xu and H. Y. Chen, *Anal. Chem.*, 2019, **91**(18), 12000–12005.
72 P. Miao, Y. Sun, G. Zheng, B. Wang, W. Wang, J. Zhang, M. Yan and Y. Lv, *J. Colloid Interface Sci.*, 2024, **667**, 82–90.
73 A. Khodadoust, N. Nasirizadeh, S. M. Seyfati, R. A. Taheri, M. Ghanei and H. Bagheri, *Talanta*, 2023, 252.
74 W. Cimmino, D. Migliorelli, S. Singh, A. Miglione, S. Generelli and S. Cinti, *Anal. Bioanal. Chem.*, 2023, **415**(18), 4511–4520.
75 Sigma-Aldrich. Urea solution, synthetic, product number SAE0074 – Safety Data Sheet (SDS). https://www.sigmaaldrich.com/TR/en/product/sigma/sae0074, accessed October 2025.
76 F. Mafakheri, A. Asakereh, S. Khoee and M. Kamankesh, *Sci. Rep.*, 2023, **13**(1), 10326.
77 Wikipedia, Urease, https://en.wikipedia.org/wiki/Urease, accessed October 2025.
78 A. Alinezhad, M. Khatibi and S. N. Ashrafizadeh, *Sci. Rep.*, 2024, **14**(1), 18409.
79 A. R. Bizzarri, *Molecules*, 2024, **29**(17), 4246.
80 P. Hanczyc, *J. Phys. Chem.*, 2024, **128**(31), 7520–7529.